hydrogen

MDPI

Article

The Synergistic Effects of Alloying on the Performance and Stability of Co_3Mo and Co_7Mo_6 for the Electrocatalytic Hydrogen Evolution Reaction

Youyi Sun and Alexey Y. Ganin *

School of Chemistry, University of Glasgow, Glasgow G12 8QQ, UK; y.sun.2@research.gla.ac.uk
* Correspondence: alexey.ganin@glasgow.ac.uk; Tel.: +44-0141-330-8404

Received: 27 August 2020; Accepted: 8 October 2020; Published: 10 October 2020

Abstract: Metal alloys have become a ubiquitous choice as catalysts for electrochemical hydrogen evolution in alkaline media. However, scarce and expensive Pt remains the key electrocatalyst in acidic electrolytes, making the search for earth-abundant and cheaper alternatives important. Herein, we present a facile and efficient synthetic route towards polycrystalline Co_3Mo and Co_7Mo_6 alloys. The single-phased nature of the alloys is confirmed by X-ray diffraction and electron microscopy. When electrochemically tested, they achieve competitively low overpotentials of 115 mV (Co_3Mo) and 160 mV (Co_7Mo_6) at 10 mA cm^{-2} in 0.5 M H_2SO_4, and 120 mV (Co_3Mo) and 160 mV (Co_7Mo_6) at 10 mA cm^{-2} in 1 M KOH. Both alloys outperform Co and Mo metals, which showed significantly higher overpotentials and lower current densities when tested under identical conditions, confirming the synergistic effect of the alloying. However, the low overpotential in Co_3Mo comes at the price of stability. It rapidly becomes inactive when tested under applied potential bias. On the other hand, Co_7Mo_6 retains the current density over time without evidence of current decay. The findings demonstrate that even in free-standing form and without nanostructuring, polycrystalline bimetallic electrocatalysts could challenge the dominance of Pt in acidic media if ways for improving their stability were found.

Keywords: hydrogen evolution reaction; metal alloys; water electrolysis; acidic conditions

1. Introduction

The share of wind and solar in global electricity output has reached 9% in Q1 2020 [1,2]. It is largely anticipated that the output from renewables will continue to grow over the next decade. This presents a substantial challenge to distribution networks due to the intermittent nature of renewable energy. Batteries have been considered an efficient way of moderating daily changes in electricity production, but they discharge quickly and hence are currently unable to provide a long-term solution for managing the electricity output between the seasons [3]. Storing the excess renewable electricity directly as fuels, for example, from photovoltaic cells during summer and then using these fuels later during cold and short winter days could be a practical way to address this challenge.

Hydrogen (with a world demand of over 70 Mt per year in 2018 [4–6]) is an excellent fuel and key feedstock in the production of chemicals and fertilisers. However, less than 0.1% of global hydrogen currently comes from water electrolysis. This can change rapidly if electrolysis is used as a storage platform for mitigating seasonal variations in electricity output rather than as a stand-alone method of H_2 production [7]. In an electrochemical cell (which is an integral part of any industrial electrolyser), water electrolysis yields best its results in alkaline and acidic electrolytes. Hydrogen evolves at a cathode, and thus the choice of cathode materials (which simultaneously act as electrocatalysts) is crucial for driving the hydrogen evolution reaction (HER) from water at appreciable voltage and current

density rates [8]. Industrial alkaline electrolysers (AEL) with an energy output as high as 6 MW [7] have already benefited from the early adoption of low-cost Ni-based alloys as cathode materials [5–10]. Pt-group metals, on the other hand, remain the only viable choice in acidic conditions [11,12]. Platinum contributes to the costs of proton-exchange membrane electrolysers (PEMEL), which are almost twice as expensive per KWh as AEL [7]. With the PEMEL offering short start-up times and load-flexibility (which are significant parameters for the integration with renewable energy networks), reducing the cost of PEMEL is important. Finding earth-abundant alternatives to Pt in acidic conditions is thus the key to future integration of PEMEL into renewable networks and more research is needed in this context.

Metal alloys show electrocatalytic performance superior to their individual metal counterparts [13–15]. This synergetic effect has been successfully exploited in alkaline electrolytes [7,9,15], but only limited attempts have been made to investigate the electrocatalytic performance of polycrystalline products with well-defined structures and compositions in acidic media [16–19]. A growing interest in nanostructured materials appeals for a better understanding of the electrochemical properties of pure-phased polycrystalline alloys, and in this respect the Co–Mo system remains relatively unexplored. Coupled with the recent reports of impressive performance of Co_3Mo towards HER in 1M KOH [20,21], the investigation of electrochemical properties of alloys in the Co–Mo system is key to understanding how cheaper and more efficient electrocatalysts could be designed and made.

In this work, we investigated two binary compounds within the Co–Mo system and tested them as electrocatalysts for HER. Phase-pure, polycrystalline Co_3Mo, and Co_7Mo_6 were prepared as powders and electrochemically tested for HER in acidic and alkaline media. The tests were carried out on free-standing products directly on a glassy carbon electrode to minimize the effect of the substrate and possible impurities on their catalytic performance and electrochemical stability. There was a pronounced synergistic effect for both Co_3Mo and Co_7Mo_6 that showed substantially higher current densities compared with Co and Mo metals. However, polycrystalline free-standing Co_3Mo has a poor electrochemical stability. This makes it a suboptimal choice as an electrocatalyst compared with Co_7Mo_6, which retained its performance after prolonged hours of testing.

2. Experimental Section

2.1. Synthesis

$CoMoO_4$ precursor was made from $Na_2MoO_4{\cdot}2H_2O$ (Sigma-Aldrich, Gillingham, UK 99.99%) and $CoCl_2{\cdot}6H_2O$ (Alfa Aesar, Lancashire, UK 99.9%). First, $Na_2MoO_4{\cdot}2H_2O$ (1 g; 4.13 mmol; 1.00 eq.) was dissolved in 75 mL of deionized water in a 200 mL beaker and stirred at 400 rpm to produce a clear, 0.55 M solution. In a separate 200 mL beaker, $CoCl_2{\cdot}6H_2O$ (0.983 g, 4.13 mmol, 1.00 eq.) was dissolved in 75 mL of water to produce a 0.55 M solution as well. The $CoCl_2{\cdot}6H_2O$ solution was slowly added to the solution of $Na_2MoO_4{\cdot}2H_2O$ while stirring. The resulting solution was stirred in ambient conditions for 4 h. The solid product was then isolated on a cellulose acetate membrane filter (0.2 μm pore diameter, Sartorius, Epsom, UK) from the aqueous solution via vacuum filtration and washed with 1 L of water. The resulting powder (proved as a phase-pure $CoMoO_4$ by XRD) was dried overnight on the filter in ambient conditions and used without any additional temperature treatment.

Co_7Mo_6 was prepared in a single-step reaction between $Co(OH)_2$ (0.0080 g, 0.0861 mmol, Alfa Aesar, 99.9%) and $CoMoO_4$ (0.11294 mg, 0.5160 mmol). $Co(OH)_2$ and $CoMoO_4$ powders were mixed together with mortar and pestle. The powder mixture was sandwiched between two silica wool pieces inside a silica tube (8 mm diameter and 20 mm long). The silica tube was then placed inside a tube furnace. The reaction was carried out at 950 °C for 10 hours in 5% H_2 in Ar gas flow.

Co_3Mo was made in two steps. First, $Co(OH)_2$ (0.08492 g, 0.9136 mmol Alfa Aesar, 99.9%) and $CoMoO_4$ (0.100 g, 0.4569 mmol) were mixed together with mortar and pestle. The powder mixture was sandwiched between two silica wool pieces inside a silica tube (8 mm diameter and 20 mm long). The silica tube was then placed inside a tube furnace. The reaction was carried out at 700 °C for 10 h in

5% H_2 in Ar gas flow. The resulting powder was reground with mortar and pestle, placed back into the silica tube, and reannealed at 850 °C for 10 h in 5% H_2 in Ar gas flow.

Mo metal was made by reduction of MoO_3 (0.15 g, Sigm-Aldrich, 99.9%). MoO_3 powder was sandwiched between two silica wool pieces inside a silica tube (8 mm diameter and 20 mm long). The silica tube was then placed inside a tube furnace. The reaction was carried out at 950 °C for 10 h in 5% H_2 in Ar gas stream.

Co metal was prepared by heating $Co(OH)_2$ (0.15 g, Alfa Aesar, 99.9%). $Co(OH)_2$ powder was sandwiched between two silica wool pieces inside a silica tube (8 mm diameter and 20 mm long). The silica tube was then placed inside a tube furnace. The reaction was carried out at 350 °C for 5 h in 5% H_2 Ar stream.

2.2. Materials Characterisation

Powder X-ray diffraction (PXRD) was carried out on a Panalytical Xpert-Pro diffractometer with the Cu Kα (λ = 1.54184 Å) source operating in the Bragg-Brentano geometry. A sample was carefully spread over a zero-background holder and flattened with a glass slide. The simulation of the XRD patterns from ICSD data was carried out using Mercury 4 software [22]. The stability studies were carried out by PXRD directly on glassy carbon electrode using the fabricated bracket [23] and depicted in Figure S1.

Scanning Electron Microscopy (SEM) was performed using a Phillips XL30 ESEM instrument equipped with an Oxford Instruments X-act spectrometer for Energy Dispersive X-ray Spectroscopy (EDXS) measurements. The INCA software was used for the data analysis. Cu foil was used as the calibration standard for the EDXS. The sample preparation involved dispersing ca. 1 mg of alloy powder in 1 mL of hexane with sonication for 5 minutes. A 100 µL drop of resulting solution was casted on Cu foil, producing a well-spread and homogenous coating.

2.3. Electrochemical Characterisation

Electrocatalysts were prepared in the form of inks, which were loaded onto polished glassy carbon electrodes, for catalytic testing. To prepare the catalytic ink, 8 mg of a synthesised catalyst was added to a mixture of 1.00 mL of DMF (99.9%, Sigma-Aldrich) and 50 µL of Nafion (5 wt. % in mixture of lower aliphatic alcohols and water, Sigma-Aldrich) followed by sonication for half an hour. Then, 30 µL of the prepared inks were applied onto the surface of polished glassy carbon electrodes with a surface area of 0.071 cm^2 (corresponding to sample loading of ca. 3.3 mg $cm^{-2}_{geometric}$) and left to dry overnight. A Biologic SP-150 potentiostat with a three-electrode setup was used to investigate the electrochemical performance. The prepared electrode was used as a working electrode, and carbon felt and 3 M Ag/AgCl were used as counter and reference electrodes, respectively. The catalytic activity towards the HER was tested in 0.5 M H_2SO_4 (prepared by dilution of 95% H_2SO_4, Fischer, Wallingford, UK, with deionised water) and 1 M KOH (prepared from 85% KOH, Honeywell, UK) for all materials. The electrode potentials were converted to reversible hydrogen electrode (RHE) by E(RHE) = E(Ag/AgCl) + 0.209V + 0.059 × pH value, and the ohmic resistances were compensated. Polarization curves (obtained using linear sweep voltammetry (LSV) and cyclic voltammetry (CV)) were set up in a single-compartment electrochemical cell, and performed with a scan rate of 5 mV s^{-1} and 100 mV s^{-1}. Tafel plots were obtained from the polarisation data.

2.4. Gas Chromatography Measurements

Gas chromatography (GC) was used to confirm the production of hydrogen using an Agilent GC 7890A instrument with a thermal conductivity detector. The column used was a 30 meter-long 0.320 mm widebore HP-molesieve column (Agilent). The GC oven temperature was set to 27 °C, and the carrier gas was Ar. The front inlet was set to 100 °C. The hydrogen production was experimentally measured using a single cell two-electrode set up (Figure S2), which involved the catalyst-deposited on a glassy carbon working electrode and carbon felt counter electrode attached to a silver wire immersed

in 0.5 M H_2SO_4. A constant volume of electrolyte was used in order to keep the cell headspace accurate. The cell was then sealed with a septum and flushed with Ar for 30 minutes. A representative 25 µL sample of the headspace was taken with a syringe and injected into the GC. No hydrogen peak was detected on the chromatogram at this stage. The flow of Ar was stopped, and galvanostatic electrolysis was then performed with an applied current of −0.24 mA. At regular intervals, a representative 25 µL sample of the headspace was taken with a syringe and probed by the GC. The experimental volume% of H_2 in the cell headspace was calculated from the comparison of the hydrogen peak areas detected by GC and the peak area detected by GC on certified standards of hydrogen at various % concentrations in Ar (CK Gas Products Limited, UK) before the electrolysis. The detection on certified standards was carried out as follows. The cell sealed with a septum was flushed with a standard for 30 min, and then a representative 25 µL sample of the headspace was taken with a syringe and injected into the GC. The expected volume percentages of hydrogen in the headspace was calculated by converting the charge passed to an expected number of moles of gas, taking the volume of 1 mole of an ideal gas at room temperature and pressure to be 24.5 L.

3. Results and Discussion

The phase diagram of Co-Mo is well established [24–27]. Initial attempts were made to make Co_3Mo from $CoMoO_4$ as described in [20]. However, only formation of Co_7Mo_6 with Mo as an impurity (in line with the nominal Co:Mo = 1:1 composition in $CoMoO_4$) was observed within tested temperature ranges of 700–950 °C. Therefore, the reaction of mixtures of $CoMoO_4$ and $Co(OH)_2$ was used instead of a single $CoMoO_4$ precursor. This proved to be a successful strategy for synthesis, and produced phase-pure products. Therefore, all samples reported in this work were made by this route as also described in the experimental section.

The PXRD pattern of Co_3Mo (Figure 1a) prepared at 850 °C shows a very good match with the simulated patterns for hexagonal Co_3Mo [28]. The attempts to prepare Co_3Mo at higher temperatures (to match the reaction temperature with the one used for synthesis of Co_7Mo_6 for a better comparison between two alloys) led to phase separation with Co and Co_7Mo_6 as impurities. Therefore, the temperature of 850 °C was deemed optimal. The attempt to carry out the reaction at higher temperatures was motivated by the assumption that products prepared at similar temperatures are more likely to have similar morphologies and surface areas. Hence, a comparatively more reliable assessment of their electrochemical performance would be possible.

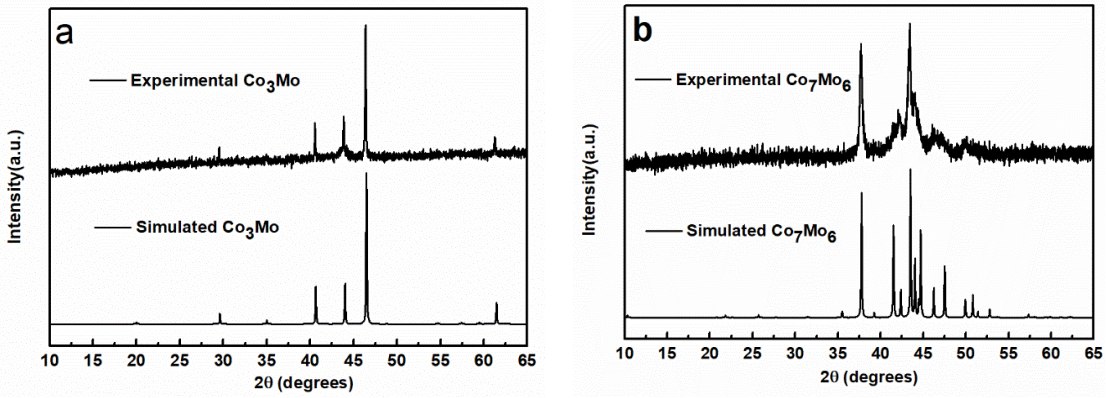

Figure 1. Powder XRD patterns of phase-pure alloys: (**a**) Co_3Mo prepared at 850 °C and matched against simulated pattern from ICSD database (624214) and (**b**) Co_7Mo_6 prepared at 950 °C matched against simulated pattern from ICSD database (624213).

The formation of phase-pure rhombohedral Co_7Mo_6 was only successful at relatively high temperature of 950 °C, as evident from the powder X-ray diffraction, which matched very well with the peak positions of the simulated pattern for Co_7Mo_6 from the inorganic crystal structure database

(ICSD) [29]. The lower intensity of some peaks, especially the peak at ca. 42.5°, when compared with the simulated pattern was probably due to peak broadening caused by disorder (stacking faults) within the rhombohedral structure of Co_7Mo_6 [30–32]. Lower reaction temperatures used for synthesis of Co_7Mo_6 always resulted in elemental Mo impurities.

The reader may have noticed from the experimental part that both Co and Mo used as controls were prepared by reduction in H_2/Ar stream from $Co(OH)_2$ and MoO_3 (rather than using elemental Co and Mo purchased from the suppliers of chemicals). The rationale behind this approach was based on an assumption that it would provide a more adequate comparison with Co_7Mo_6 and Co_3Mo, which were made under reductive conditions from $CoMoO_4$ and $Co(OH)_2$. Both Co and Mo are single phase products according to PXRD (Figures S3 and S4).

The morphology of Co_3Mo from the SEM (Figure 2a and Figure S5 for a higher magnification image) could be described as consisting of spherical-shaped particles with a diameter of ca. 300–500 nm. The microstructure of Co_3Mo is substantially different from the morphology of $CoMoO_4$ precursor, which consisted of well-defined prismatic microcrystals (Figure S6). On the other hand, there is a certain degree of similarity between the morphology of Co_3Mo synthesized in this work and Co_3Mo prepared on Cu-substrate by dealloying Cu from an arc-melted product in sulfuric acid [21] and by reduction of freeze-dried metal oxides in 8% H_2/Ar gas mixture [32]. The SEM images in [21,32] display the aggregates of the spherical particles similar to those observed in the current work.

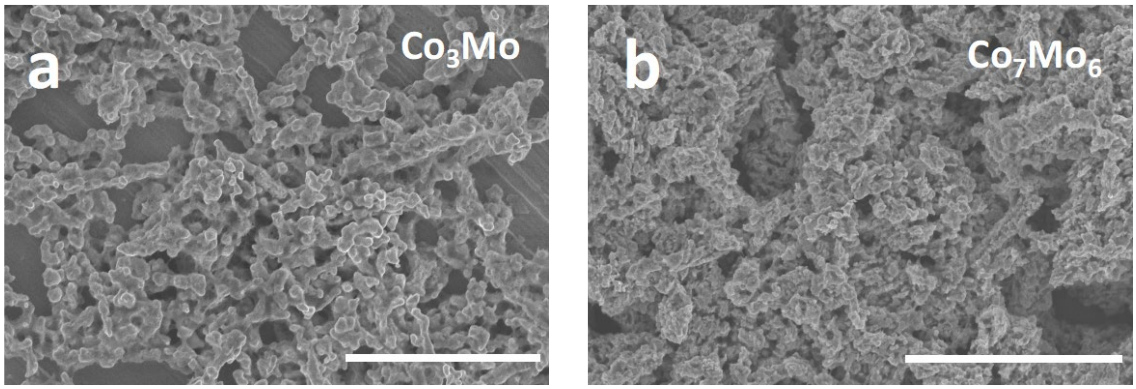

Figure 2. Scanning electron microscopy (SEM) images of Co_3Mo and Co_7Mo_6: (**a**) Co_3Mo prepared at 850 °C and (**b**) Co_7Mo_6 prepared at 950 °C. The scale bars on both images correspond to 5 μm.

Co_7Mo_6 showed similar microstructure to Co_3Mo, although with less-defined crystallite shapes and less apparent surface roughness (Figure 2b). This similarity between Co_3Mo and Co_7Mo_6 surfaces is even more pronounced at lower magnification (Figure S7), with Co_3Mo appearing more porous. The difference is unsurprising, given that the higher synthetic temperature was used for Co_7Mo_6, which could have led to sintering and coalescence of particles [32].

Energy dispersive X-ray spectroscopy (EDXS) confirmed that Co_3Mo and Co_7Mo_6 are homogenous (Table 1). The average compositions are in line with the expected theoretical compositions within the error of the measurements. The higher Mo content within the samples could be explained by the overlap between Cu (0.93 eV, L_α) and Co (0.76 eV, L_α), peaks which lead to underestimation of Co peak areas (Figure S8). The Cu-peak was due to the X-ray beam penetrating down to Cu foil, which was used as a support for drop-casted sample in EDXS characterization.

Table 1. Elemental analysis of Co_3Mo and Co_7Mo_6 by EDXS. The results are the average of values collected from several points across a sample, and the errors present the standard deviations between the values at these points.

	Co_3Mo		Co_7Mo_6	
	Co	**Mo**	**Co**	**Mo**
at. % Exp.	73.57 ± 1.79	28.5 ± 2.1	50.55 ± 0.82	49.5 ± 0.82
at. % Theory	75	25	53.8	46.2

After establishing the purity of the samples, linear sweep voltammetry (LSV) was used to investigate electrocatalytic activity of Co_3Mo and Co_7Mo_6 (Figure 3a). At the current density of 10 mA cm^{-2} (which has been suggested as a useful benchmark in conjunction with photovoltaic applications [8]), the overpotential values of 115 ± 8 mV and 160 ± 5 mV are achieved for Co_3Mo and Co_7Mo_6, respectively (Figure 3a). At the same current density, Mo and Co show significantly higher overpotentials of 373 ± 7 mV and 411 ± 5 mV, respectively. Furthermore, upon application of a reductive bias in 0.5 H_2SO_4 both alloys achieved much higher current densities (Figure S9) than elemental Co and Mo powders. The observed overpotentials confidently place both Co_3Mo and Co_7Mo_6 among the best catalysts for HER from water in acidic electrolytes [8,14,15].

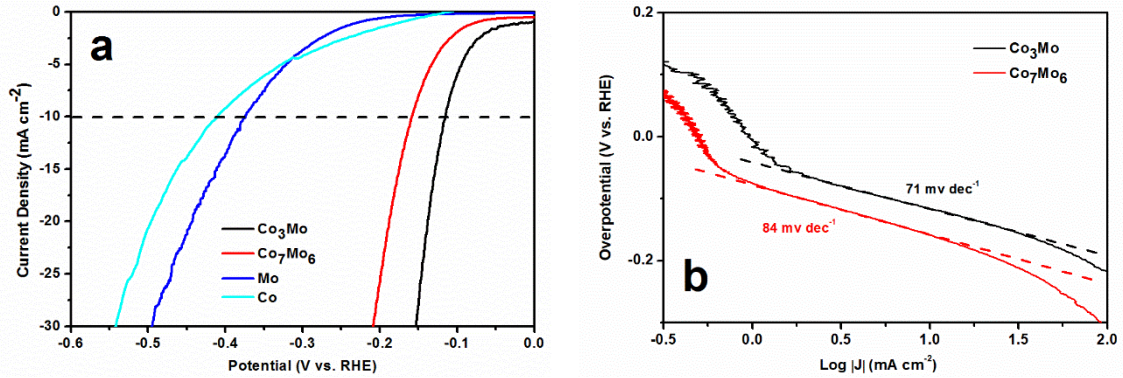

Figure 3. Electrochemical studies of Co_3Mo and Co_7Mo_6: (**a**) comparison of current densities achieved by Co_3Mo, Co_7Mo_6, as well as Mo and Co powders in 0.5 M H_2SO_4. The dashed line indicates a current density of 10 mA cm^{-2} (**b**) Tafel plots and corresponding Tafel slopes of Co_3Mo and Co_7Mo_6 in 0.5 M H_2SO_4.

Tafel plots were studied to investigate the possible kinetics of the reaction (Figure 3b). However, the resulting Tafel slope values of 71 ± 7 mV dec^{-1} (Co_3Mo) and 84 ± 5 mV dec^{-1} (Co_7Mo_6) are outside the values for defined reaction mechanisms, i.e., 40 mV dec^{-1} (Volmer-Heyrovsky) and 120 mV dec^{-1} (Volmer) [8,33]. The deviation from ideal Tafel slopes is a common situation with powdered materials and Co_3Mo in particular [8,20,33], as they do not always follow perfect charge-transfer behaviour (Tafel behaviour) due to mass transport effects [34]. Proper accounting for mass transport effects requires comprehensive numerical simulation procedures that are beyond the scope of this manuscript.

An initial assessment of morphology by SEM indicated a denser Co_7Mo_6 sample. This could lead to a relative underperformance of Co_7Mo_6 in comparison with more porous Co_3Mo due to a lower surface area, which leads to a lower specific activity [34]. We attempted measurements of surface area using N_2 gas adsorption. However, the sorption characteristics of both samples were below the detection limit of the instrument due to the low surface area of the samples. An alternative option would be to investigate the surface area using Kr gas (instead of N_2), which was shown as an efficient approach in the case of Ni-Mo alloys [35]. However, our group lacks access to such equipment. Therefore, we used values of double-layer capacitance (C_{DL}) for the comparison of the relative surface areas between the two alloys. C_{DL} has been deemed to be proportional to roughness factor and

therefore is routinely used as an approximation for the electrochemical surface area of a sample in the absence of direct physical data [36–38]. The C_{DL} values were evaluated at a constant potential from the difference of current densities with the scan rate (Figure 4a).

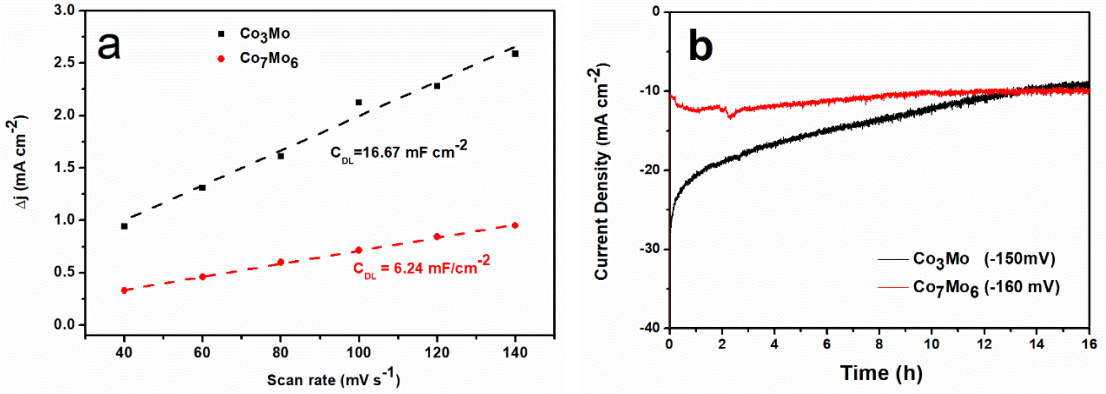

Figure 4. Evaluation of double-layer capacitance and stability of Co_3Mo and Co_6Mo_7: (**a**) current density differences of Co_3Mo and Co_7Mo_6 plotted against scan rates. The capacitance currents were measured at 300 mV vs. normal hydrogen electrode (NHE). (**b**) Controlled-potential chronoamperometry profiles of Co_3Mo and Co_7Mo_6 in 0.5 M H_2SO_4 at the applied potentials of 150 and 160 mV, respectively.

The ratio between $C_{DL}(Co_3Mo)$:$C_{DL}(Co_7Mo_6)$ = 2.7 indicates that the surface area of Co_3Mo could be three times higher than that of Co_7Mo_6, although in the absence of direct measurements of surface area (such as gas sorption) this value should be treated with great caution [39]. For example, Csernica et al. noticed that although the ratio between Kr BET surface area of their Mo_7Ni_7 and $Ni_{0.92}Mo_{0.08}$ varied almost by a factor of 4, the C_{DL} ratio between these sample was only 1.6 [35]. Still, in the absence of Kr BET data, the comparison between C_{DL} numbers appears as a good approximation of surface areas (as it seems to give numbers of the same magnitude as BET data). The comparison of C_{DL} also corroborates with SEM results, which pointed out that Co_3Mo is more porous than Co_7Mo_6. Therefore, given the fact that the mass loadings and electrode surface area were identical, we can assume that the relative surface area of Co_3Mo is 2.7 times higher than Co_7Mo_6. Thus, the specific activity of Co_7Mo_6 (mA $cm^{-2}{}_{catalyst}$) is 2.7 times higher. In other words, based on this approximation Co_7Mo_6 can deliver 2.7 times higher current densities, as demonstrated in Figures S10 and S11, which also leads to an improved overpotential of 123 mV at 10 mA cm^{-2}. This is an interesting result, especially given that recent DFT calculations on Co_3Mo have shown that Mo-atoms are the catalytic sites in Co_3Mo [20]. One can assume that increasing the amount of Mo would lead to improved catalytic performance. However, due to differences in crystal structures of Co_3Mo and Co_7Mo_6, it is hard to draw definitive conclusions at this stage and further computational studies are required.

The stability of the catalysts was tested by applying a constant potential over time (Figure 4b). There is a clear decline in current densities for Co_3Mo, while Co_7Mo_6 retained the original values over 16 h of testing without any evidence of decay. Co_7Mo_6 also shows a good stability upon cycling for 1000 times to the current densities of over 100 mA cm^{-2} at a scan rate of 100 mV s^{-1} (Figure S12). The stability of Co_3Mo was additionally investigated by powder XRD with the product measured before and after electrolysis directly on a glassy carbon electrode (Figure S13). The disappearance of a peak at ca. 43.8° and significant reduction of peak at ca. 46.3° suggest the decomposition of the product. We can hypothesize that the prolonged electrolysis leads to formation of metal hydrides and dissolution of the product based on a previous report for Ni-based catalysts [40].

To the best of our knowledge, this is the first report of the electrocatalytic performance of Co_7Mo_6, and therefore, it is important to prove that the LSV measurements correspond to the actual reduction of protons to hydrogen. A representative trace of gas produced in an airtight cell and probed by gas chromatography is shown in Figure S14, which confirms the production of hydrogen using Co_7Mo_6.

There are currently no electrochemical studies of Co_3Mo in acidic conditions, and to the best of our knowledge no studies of Co_7Mo_6 in acidic or alkaline media. Therefore, to put the results into perspective we studied Co_3Mo and Co_7Mo_6 by LSV in 1 M KOH (Figure S15). The alloys show overpotentials of 120 ± 5 mV (Co_3Mo) and 160 ± 5 mV (Co_7Mo_6) at 10 mA cm^{-2}. In comparison with recently reported Co_3Mo on nickel foam, the observed overpotential seems high [20]. Chen et al. reported the overpotentials of 78 mV (C_{DL} = 15.8 mF cm^{-2}) and 75 mV (C_{DL} = 17.5 mF cm^{-2}). However, the C_{DL} = 3.2 mF cm^{-2} observed for Co_3Mo in this work (based on double-layer capacitance in 1M KOH) is lower, and this could explain the higher overpotential (Figure S16). The comparison also points out the limitation of using double-layer capacitance (C_{DL}) as a proxy for the catalytic surface area. Without direct measurement of surface area, it is hard to tell whether it is the substrate or other factors (such as substantially higher surface area due to nanostructuring) that led to such a difference in the overpotential values. Still C_{DL} is a useful parameter, as it at least provides some background information that enables a comparison between samples prepared in different labs. For example, Co_3Mo prepared by arc-melting showed an overpotential of 340 mV at 10 mA cm^{-2} in 1M KOH [41]. However, since this work is missing C_{DL} values, it is difficult to explain the high value of overpotential. Conversely, nanoporous Co_3Mo on Cu substrate achieved 65 mV cm^{-2} at 100 mA cm^{-2} [21] but the material had a C_{DL} = 324 mF cm^{-2}. The Tafel slope of 40 mA cm^{-2} suggests an overpotential of just 25 mV cm^{-2} at 10 mA cm^{-2} in 1 M KOH. However, given a large C_{DL} it appears that the overpotential may be underestimated. Therefore, it is often difficult to decouple the role of the substrate and morphology from the actual performance of the material, and more research on free-standing catalysts is needed. Remarkably, Co_7Mo_6 achieved substantially higher current densities in 1 M KOH (well in excess of 120 mA cm^{-2}) than in 0.5 H_2SO_4 (Figure S17). It also outperformed, in this respect, Co_3Mo as well as Co and Mo powders.

We also studied Tafel plots of Co_3Mo and Co_7Mo_6 (Figure S18), which showed the Tafel slopes of 117 mV dec^{-1} (Co_3Mo) and 106 mV dec^{-1} (Co_7Mo_6). The values suggest that the electron transfer reaction leading to H-adsorption on the surface of the catalyst is the rate determining step [8,33]. The Tafel slope for Co_3Mo is broadly consistent with arc-melted Co_3Mo (105 mV dec^{-1}) [41] and Co_3Mo on Ni-foam [20], although it should be noted that in [20] the Tafel slopes varied quite significantly depending on the synthesis reaction times and C_{DL} values. Conversely, nanostructured Co_3Mo on Cu substrate showed substantially different Tafel slope of 40 mV dec^{-1} [21]. This reinforces the fact that the morphology and support material could play a vital role (as well as adding an extra layer of complexity) when it comes to comparison between products made in different labs.

Finally, we also evaluated the stability of free-standing Co_3Mo in 1M KOH to see how it compared with the products prepared on metal supports (Figure S19). Contrary to the previous reports [20,21] (which reported good stability of Co_3Mo on Ni-foam and Cu substrate), we observed a clear fading of the current with time. This suggests that substrate plays a significant role. Therefore, this work (of free-standing systems decoupled from the support) provides an important study that should provide a better general understanding of the actual catalyst's performance.

4. Conclusions

In conclusion, phase-pure Co_3Mo and Co_7Mo_6 can be prepared through the reaction of stoichiometric amounts of $Co(OH)_2$ and $CoMoO_4$. The evaluation of electrochemical performance points out that Co_3Mo in the free-standing form could routinely show good catalytic performance similar to previously studied classes of materials in acidic conditions. To the best of our knowledge, this is the first report on the activity of Co_7Mo_6 towards HER either in acidic or alkaline conditions. When adjusted for the C_{DL} ratios, Co_7Mo_6 demonstrated improved current densities and an overpotential of 123 mV at 10 mA cm^{-2} tentatively, suggesting that it can be as electrocatalytically active as Co_3Mo while showing a better stability in acidic media. However, without accounting for surface areas by other methods, these results should be treated with caution. This highlights a set of challenges for researchers working on nanostructured catalysts. The issue is quite evident from the comparison between free-standing

Co_3Mo investigated in this work and Co_3Mo fabricated on Ni-foam or Cu substrates when tested in 1 M KOH. Therefore, the estimation of surface area by direct physical methods (i.e., through gas adsorption which is independent of sample history, oxidation state and solvent effects) is strongly recommended for an adequate comparison between products made in different labs. Computational studies are also promising for clarification whether the difference in comparative performance of Co_3Mo and Co_7Mo_6 fundamentally persists, and these will be explored in our future work. In particular, the studies of the mechanisms of charge-transfer and proton reduction behavior are considered as the most appropriate.

Supplementary Materials: The following are available online at http://www.mdpi.com/2673-4141/1/1/2/s1, Figure S1: PRXD bracket for testing of catalyst directly on the electrode. Figure S2: Electrochemical cell used for hydrogen production measurements. Figure S3: PXRD patterns of Mo. Figure S4: Powder XRD patterns of Co. Figure S5: Higher magnification SEM image of Co_3Mo. Figure S6: SEM image of $CoMoO_4$ precursor. Figure S7: Low magnification SEM image of Co_3Mo and Co_7Mo_6. Figure S8: A representative EDXS spectrum of Co_3Mo sample. Figure S9: Comparison of current densities achieved by Co_3Mo, Co_7Mo, Co and Mo. Figure S10: Comparison of current densities achieved by Co_3Mo, Co_7Mo_6 and Co_7Mo_6 when adjusted for results of double-layer capacitance (C_{DL}). Figure S11: Magnified version of Figure S10. Figure S12: Comparison of current densities achieved by Co_7Mo_6 in 0.5M H_2SO_4 before and after 1000 scans at the scan rate of 100 mv s^{-1}. Figure S13: Comparison of XRD pattern achieved by Co_3Mo in 0.5M H_2SO_4 before and after 1000 scans at the scan rate of 100 mv s^{-1}. Figure S14: A representative trace of the proportion of H_2 (in vol. %) in the single-cell headspace during the electrolysis of Co_7Mo_6. Figure S15: Comparison of current densities achieved by Co_3Mo, Co_7Mo_6 as well as Mo and Co powders in 1M KOH. Figure S16: Evaluation of double-layer capacitance of Co_3Mo and Co_7Mo_6 achieved in 1 M KOH. Figure S17: Extended range of the Graph in Figure S15. Figure S18: Tafel plots and corresponding Tafel slopes of Co_3Mo and Co_7Mo_6 in 1M KOH. Figure S19: Controlled-potential chronoamperometry profile of Co_3Mo and Co_7Mo_6 in 1 M KOH under applied voltage corresponding to current densities of ca. 10 mA cm^{-2}.

Author Contributions: A.Y.G. conceived and managed the experiments. Y.S. designed the experiments and carried them out. Y.S. and A.Y.G. analysed and plotted the data. A.Y.G. wrote the manuscript. All authors have read and agreed to the published version of the manuscript.

Funding: Parts of this research was funded by The Carnegie Trust for a Research Incentive Grant (RIG007428). China Scholarship Council (CSC) funded the CSC scholarship to Y.S.

Acknowledgments: A.Y.G. acknowledges the Carnegie Trust for a Research Incentive Grant and the University of Glasgow for supporting this work. Y.S. thanks China Scholarship Council for providing him with the scholarship.

Conflicts of Interest: The authors declare no conflict of interests. The funders had no role in the design of the study; in the collection, analyses, or interpretation of data; in the writing of the manuscript; or in the decision to publish the results.

References

1. *IEA Global Energy Review 2020*; IEA: Paris, France, 2020; Available online: https://www.iea.org/reports/global-energy-review-2020 (accessed on 26 August 2020).
2. *IEA Monthly Electricity Statistics*; IEA: Paris, France, 2020; Available online: https://www.iea.org/reports/monthly-electricity-statistics (accessed on 25 September 2020).
3. Fan, X.; Liu, B.; Liu, J.; Ding, J.; Han, X.; Deng, Y.; Lv, X.; Xie, Y.; Chen, B.; Hu, W.; et al. Battery Technologies for Grid-Level Large-Scale Electrical Energy Storage. *Trans. Tianjin Univ.* **2020**, *26*, 92–103. [CrossRef]
4. *IEA The Future of Hydrogen*; IEA: Paris, France, 2019; Available online: https://www.iea.org/reports/the-future-of-hydrogen (accessed on 26 August 2020).
5. Chehade, Z.; Mansilla, C.; Lucchese, P.; Hilliard, S.; Proost, J. Review and analysis of demonstration projects on power-to-X pathways in the world. *Int. J. Hydrogen Energy* **2019**, *44*, 27637–27655. [CrossRef]
6. Baroutaji, A.; Wilberforce, T.; Ramadan, M.; Olabi, A.G. Comprehensive Investigation on Hydrogen and Fuel Cell Technology in the Aviation and Aerospace Sectors. *Renew. Sustain. Energy Rev.* **2019**, *106*, 31–40. [CrossRef]
7. Buttler, A. Current status of water electrolysis for energy storage, grid balancing and sector coupling via power-to-gas and power-to-liquids: A review. *Renew. Sustain. Energy Rev.* **2018**, *82*, 2440–2454. [CrossRef]
8. Roger, I.; Shipman, M.A.; Symes, M.D. Earth-abundant catalysts for electrochemical and photoelectrochemical water splitting. *Nat. Rev. Chem.* **2017**, *1*, 1–13. [CrossRef]

9. Sequeira, C.A.C.; Cardoso, D.S.P.; Amaral, L.; Šljukić, B.; Santos, D.M.F. On the performance of commercially available corrosion-resistant nickel alloys: A review. *Corros. Rev.* **2016**, *34*, 187–200. [CrossRef]
10. Keçebaş, A.; Kayfeci, M.; Bayat, M. Electrochemical hydrogen generation. In *Solar Hydrogen Production: Processes, Systems and Technologies*; Elsevier: Amsterdam, The Netherlands, 2019; pp. 299–317. [CrossRef]
11. Kongkanand, A.; Mathias, M.F. The Priority and Challenge of High-Power Performance of Low-Platinum Proton-Exchange Membrane Fuel Cells. *J. Phys. Chem. Lett.* **2016**, *7*, 1127–1137. [CrossRef] [PubMed]
12. Rajan, A.G.; Martinez, J.M.P.; Carter, E.A. Why Do We Use the Materials and Operating Conditions We Use for Heterogeneous (Photo)Electrochemical Water Splitting? *ACS Catal.* **2020**, *10*, 11177–11234. [CrossRef]
13. Jaksic, M.M. Hypo-Hyper-d-Electronic Interactive Nature of Interionic Synergism in Catalysis and Electrocatalysis for Hydrogen Reactions. *Int. J. Hydrogen Energy* **2001**, *26*, 559. [CrossRef]
14. Rößner, L.; Armbrüster, M. Electrochemical Energy Conversion on Intermetallic Compounds: A Review. *ACS Catal.* **2019**, *9*, 2018–2062. [CrossRef]
15. Schalenbach, M.; Zeradjanin, A.R.; Kasian, O.; Cherevko, S.; Mayrhofer, K.J.J. A Perspective on Low-Temperature Water Electrolysis –Challenges in Alkaline and Acidic Technology. *Int. J. Electrochem. Sci.* **2018**, *13*, 1173–1226. [CrossRef]
16. Highfield, J.G.; Claude, E.; Oguro, K. Electrocatalytic Synergism in Ni/Mo Cathodes for Hydrogen Evolution in Acid Medium: A New Model. *Electrochim. Acta* **1999**, *44*, 2805. [CrossRef]
17. Jin, D.; Yu, A.; Lee, Y.; Kim, M.H.; Lee, C. Ni_xRh_{1-x} bimetallic alloy nanofibers as a pH-universal electrocatalyst for the hydrogen evolution reaction: The synthetic strategy and fascinating electroactivity. *J. Mater. Chem. A* **2020**, *8*, 8629–8637. [CrossRef]
18. Nsanzimana, J.M.V.; Peng, Y.; Miao, M.; Reddu, V.; Zhang, W.; Wang, H.; Xia, B.Y.; Wang, X. An Earth-Abundant Tungsten–Nickel Alloy Electrocatalyst for Superior Hydrogen Evolution. *ACS Appl. Nano Mater.* **2018**, *1*, 1228–1235. [CrossRef]
19. Schalenbach, M.; Speck, F.D.; Ledendecker, M.; Kasiana, O.; Goehl, D.; Mingers, A.M.; Breitbach, B.; Springer, H.; Cherevko, S.; Mayrhofer, K.J.J. Nickel-molybdenum alloy catalysts for the hydrogen evolution reaction: Activity and stability revised. *Electrochimica Acta* **2018**, *259*, 1154–1161. [CrossRef]
20. Chen, J.; Ge, Y.; Feng, Q.; Zhuang, P.; Chu, H.; Cao, Y.; Smith, W.R.; Dong, P.; Ye, M.; Shen, J. Nesting Co_3Mo Binary Alloy Nanoparticles onto Molybdenum Oxide Nanosheet Arrays for Superior Hydrogen Evolution Reaction. *ACS Appl. Mater. Interfaces* **2019**, *11*, 9002. [CrossRef]
21. Shi, H.; Zhou, Y.T.; Yao, R.Q.; Wan, W.B.; Ge, X.; Zhang, W.; Wen, Z.; Lang, X.Y.; Zheng, W.T.; Jiang, Q. Spontaneously Separated Intermetallic Co_3Mo from Nanoporous Copper as Versatile Electrocatalysts for Highly Efficient Water Splitting. *Nat. Commun.* **2020**, *11*, 1. [CrossRef]
22. Macrae, C.F.; Sovago, I.; Cottrell, S.J.; Galek, P.T.A.; McCabe, P.; Pidcock, E.; Platings, M.; Shields, G.P.; Stevens, J.S.; Towler, P.A. Wood, Mercury 4.0: From visualization to analysis, design and prediction. *J. Appl. Cryst.* **2020**, *53*, 226–235. [CrossRef]
23. McGlynn, J.C.; Friskey, M.; Ganin, A.Y. Parameter Optimisation for Electrochemically Activated $MoTe_2$. *Sustain. Energy Fuels* **2020**, *4*, 4473–4477. [CrossRef]
24. Raydt, U.; Tammann, G. Alloys of molybdenum and cobalt. *Z. Anorg. Allg. Chem.* **1914**, *83*, 246–252. [CrossRef]
25. Takei, T. Equilibrium diagram of the cobalt-molybdenum system. *J. Study Metals* **1928**, *5*, 364–376.
26. Sykes, W.P.; Graff, H.F. The cobalt-molybdenum system. *T. Am. Soc. Metal.* **1935**, *23*, 249–283.
27. Hashimoto, U. Effect of additions to cobalt on its allotropic transformation. *Nippon Kinzoku Gakkaishi* **1937**, *1*, 177–189.
28. Forsyth, J.B.; D'Alte da Veiga, L.M. Refinement of the structure of the phase Co_3Mo. *Acta Cryst.* **1965**, *18*, 855–857.
29. D'Alte da Veiga, L.M. The structure of the μ-Co_7Mo_6. *Acta. Cryst.* **1962**, *15*, 543–546.
30. Sort, J.; Suriñach, S.; Muñoz, S.; Baró, D.; Wojcik, M.; Jedryka, E.; Nadolski, S.; Sheludko, N.; Nogués, J. Role of Stacking Faults in the Structural and Magnetic Properties of Ball-Milled Cobalt. *Phys. Rev. B Condens. Matter Mater. Phys.* **2003**, *68*, 014421. [CrossRef]
31. Hiraga, K.; Yamamoto, T.; Hirabayashi, M. Intermetallic compounds of the μ- and P-phases of Co_7Mo_6 studied by 1 MV Electron Microscopy. *Trans. Jpn. Inst. Met.* **1983**, *24*, 421–428. [CrossRef]
32. Vie, D.; Valero, N.; Martínez, E.; Sapiña, F.; Folgado, J.-V.A. Beltrána A new approach to the synthesis of intermetallic compounds: Mild synthesis of submicrometric Co_xM_y (M = Mo, W; x:Y = 3:1 and 7:6) particles by direct reduction of freeze-dried precursors. *J. Mat. Chem.* **2002**, *12*, 1017–1021. [CrossRef]

33. Lasia, A. Mechanism and kinetics of the hydrogen evolution reaction. *Int. J. Hydrogen Energy* **2019**, *36*, 19484–19518. [CrossRef]
34. Li, D.; Batchelor-McAuley, C.; Compton, R.G. Some thoughts about reporting the electrocatalytic performance of nanomaterials. *Appl. Mater. Today* **2020**, *18*, 100404. [CrossRef]
35. Csernica, P.M.; McKone, J.R.; Mulzer, C.R.; Dichtel, W.R.; Abruña, H.D.; DiSalvo, F.J. Electrochemical Hydrogen Evolution at Ordered Mo_7Ni_7. *ACS Catal.* **2017**, *7*, 3375–3383. [CrossRef]
36. Voiry, D.; Chhowalla, M.; Gogotsi, Y.; Kotov, N.A.; Li, Y.; Penner, R.M.; Schaak, R.E.; Weiss, P.S. Best Practices for Reporting Electrocatalytic Performance of Nanomaterials. *ACS Nano* **2018**, *12*, 9635–9638. [CrossRef] [PubMed]
37. McGlynn, J.C.; Dankwort, T.; Kienle, L.; Bandeira, N.A.G.; Fraser, J.P.; Gibson, E.K.; Cascallana-Matías, I.; Kamarás, K.; Symes, M.D.; Miras, H.N.; et al. The Rapid Electrochemical Activation of MoTe2 for the Hydrogen Evolution Reaction. *Nat. Commun.* **2019**, *10*, 4916. [CrossRef] [PubMed]
38. Benck, J.D.; Hellstern, T.R.; Kibsgaard, J.; Chakthranont, P.; Jaramillo, T.F. Catalyzing the hydrogen evolution reaction (HER) with molybdenum sulfide nanomaterials. *ACS Catal.* **2014**, *4*, 3957–3971. [CrossRef]
39. Trasatti, S.; Petrii, O.A. Real surface area measurements in electrochemistry. *J. Electroanal. Chem.* **1992**, *327*, 353–376. [CrossRef]
40. Soares, D.M. Hydride Effect on the Kinetics of the Hydrogen Evolution Reaction on Nickel Cathodes in Alkaline Media. *J. Electrochem. Soc.* **1992**, *139*, 98–105. [CrossRef]
41. Li, Y.; Ge, X.; Wang, L.; Liu, J.; Wang, Y.; Feng, L. A Free Standing Porous Co/Mo Architecture as a Robust Bifunctional Catalyst toward Water Splitting. *RSC Adv.* **2017**, *7*, 11568. [CrossRef]